Journal of Computational Physics **173,** 412–432 (2001)
doi:10.1006/jcph.2001.6863, available online at http://www.idealibrary.com on IDEAL®

Robust Multigrid Algorithms for the Navier–Stokes Equations[1]

Ruben S. Montero,† Ignacio M. Llorente,† and Manuel D. Salas‡

†*Departamento de Arquitectura de Computadores y Automática, Universidad Complutense, 28040 Madrid, Spain; and* ‡*ICASE, Mail Stop 132C, NASA Langley Research Center, Hampton, Virginia 23681-2199*
E-mail: rubensm@dacya.ucm.es; llorente@dacya.ucm.es; salas@icase.edu

Received June 6, 2000; revised June 11, 2001

Anisotropies occur naturally in computational fluid dynamics where the simulation of small-scale physical phenomena, such as boundary layers at high Reynolds numbers, causes the grid to be highly stretched, leading to a slowdown in convergence of multigrid methods. Several approaches aimed at making multigrid a robust solver have been proposed and analyzed in the literature using the scalar diffusion equation. However, they have rarely been applied to solving more complicated models, such as the incompressible Navier–Stokes equations. This paper contains the first published numerical results of the behavior of two popular robust multigrid approaches (alternating-plane smoothers combined with standard coarsening and plane-implicit smoothers combined with semi-coarsening) for solving the 3-D incompressible Navier–Stokes equations in the simulation of the driven-cavity and a boundary layer over a flat plate on a stretched grid. Grid size, grid stretching, and Reynolds number are the factors considered in evaluating the robustness of the multigrid methods. Both approaches yield large increases in convergence rates over cell-implicit smoothers on stretched grids. The combination of plane-implicit smoothers and semi-coarsening was found to be fully robust in the flat-plate simulation up to Reynolds numbers 10^6 and the best alternative in the driven-cavity simulation for Reynolds numbers above 10^3. The alternating-plane approach exhibits a better behavior for lower Reynolds numbers (below 10^3) in the driven-cavity simulation.

Key Words: plane-implicit smoothers; symmetric coupled Gauss–Seidel; robust multigrid; defect correction; Navier–Stokes.

[1] This research was supported by the National Aeronautics and Space Administration under NASA Contract NAS1-97046 while the first two authors were in residence at ICASE, NASA Langley Research Center, Hampton, VA 23681-2199. Ignacio M. Llorente and Ruben S. Montero were also supported in part by the Spanish research grant TIC 99/0474.

0021-9991/01 $35.00

1. INTRODUCTION

Multigrid techniques are generally accepted as fast and efficient methods for solving many types of partial differential equations, and particularly elliptic problems whose discretization results in a K-matrix [24]. For this kind of problem, basic point-wise iterative methods, such as Gauss–Seidel or damped Jacobi, are good smoothers, and multigrid methods exhibit an optimal complexity (work is linearly proportional to the number of unknowns), optimal memory requirements, and good parallel efficiency and scalability in parallel implementations [9].

However, the efficiency of the multigrid methods degenerates dramatically in presence of anisotropies. It is well known that in the resolution of the Poisson equation the convergence factor of the multigrid method tends to one as the anisotropies are increased [1]. Typically these anisotropies might occur when the coefficients of the discrete operator vary throughout the domain or when stretched grids are used. This anisotropic condition occurs naturally in the field of computational fluid dynamics (CFD) where the simulation of small-scale physical phenomena, such as boundary layers at high Reynolds numbers, causes the grid to be highly stretched, leading to a slowdown in convergence.

In some situations, when the source of the anisotropy is known beforehand, a block-implicit smoother can be used to improve the efficiency of the multigrid algorithm. Usually this is done by applying an implicit solver in the directions of strong coupling, as states Brandt's fundamental block relaxation rule [1]. This technique is common practice in CFD. Thomas, Diskin, and Brandt [21] have demonstrated the efficiency of the distributive smoothing scheme with line solvers applied to high Reynolds number simulations when the grid stretching is normal to the body. The benefits of plane relaxation are shown by Oosterlee in [16] for simulations of the 3-D incompressible Navier–Stokes equations over grids with nonunitary aspect ratios. Also, a combination of line-implicit techniques and semi-coarsening has been successfully used by Mavriplis in [10, 11] to solve high Reynolds number 2-D and 3-D viscous flows over anisotropic unstructured meshes.

However, in a general situation the nature of the anisotropy is not known beforehand, so there is no way of knowing which variables are coupled. Moreover, if the problem is solved on a stretched grid or the equation coefficients differ from each other throughout the domain (computational and physical anisotropy respectively) the values of the coefficients and their relative magnitudes vary for different parts of the computational domain. In such cases the multigrid techniques based on point- or plane-wise smoothers combined with full coarsening fail to smooth error components with the consequent deterioration of the multigrid convergence factor.

Several approaches aimed at making multigrid a robust solver have been proposed in the literature. One popular approach is to use standard coarsening combined with an alternating-direction implicit smoother [8, 12, 20]. This solution consists of exploring all the possibilities in order to develop a robust smoother, i.e., uses alternating-line relaxation in 2-D and alternating-plane relaxation in 3-D. Another approach to dealing with anisotropic problems is to combine an implicit smoother with an appropriate semi-coarsening procedure [4, 19]. This is rather popular in the literature and overcomes some parallelization problems that can be found in the alternating-plane smoothers [13]. For example, a simple way to avoid using an alternating-plane smoother is to use semi-coarsening in one direction and relaxation in a fixed plane (e.g., combine xy-plane relaxation with Z semi-coarsening). Other intermediate

alternatives that combine plane, line, or point relaxations with partial and full coarsening have also been presented in multigrid literature [14, 15].

Some of these robust multigrid approaches have also been tested for the efficient resolution of the 2-D Navier–Stokes equations. The alternating-direction line smoother has been investigated for the solution of the incompressible 2-D Navier–Stokes equations in [22, 17]. However, to the authors' knowledge, the robust multigrid algorithms have never been applied to the resolution of the 3-D incompressible Navier–Stokes equations. The aim of this work is to present a thorough study of the application of two common robust multigrid algorithms (alternating-plane smoothers combined with standard coarsening and plane smoothers combined with semi-coarsening) to the resolution of the 3-D Navier–Stokes equations on single-block structured grids.

The robustness of a smoother is defined as its ability to efficiently solve a wide range of problems. In this sense the definition of robustness is qualitative and has to be defined more precisely by setting up a set of suitable test problems. Traditionally, the above-mentioned approaches have shown to be robust smoothers for the anisotropic diffusion equation. In the present context we will characterize the multigrid algorithms as robust if the solution of the governing system of equations can be attained in a fixed amount of work units (computational time to discretize the partial differential equations in the finest level) independent of the grid size, grid-stretching factor, and Reynolds number. This is equivalent to saying that the convergence factor of the multigrid algorithm is independent of the grid size, stretching, and Reynolds number. We will also refer to this property as *textbook multigrid convergence* (TMC). We believe that the achievement of a textbook multigrid convergence rate through increasing the work and memory requirements per cycle is the first step to achieving *textbook multigrid efficiency* (TME). The TME, defined by Brandt in [1], fixes the computational work to solve the problem to 10 or fewer work units.

This paper is organized as follows: The numerical scheme used by our simulations is described in Section 2. Details of the implementation of the multigrid algorithm used in this work are presented in Section 3. Numerical results are obtained in Section 4 for two common benchmarks in CFD: the driven cavity and the flow over a flat plate. In this section, the robustness of the alternating-plane smoothers combined with full coarsening and plane smoothers combined with semi-coarsening will be investigated. The paper ends with some conclusions in Section 5.

2. THE PRIMITIVE EQUATIONS

The dimensionless, steady-state, incompressible Navier–Stokes equations in the absence of body forces may be written as

$$\begin{aligned} (\mathbf{u}\cdot\nabla)\mathbf{u} &= -\nabla p + \frac{1}{Re}\Delta\mathbf{u}, \\ \nabla\cdot\mathbf{u} &= 0, \end{aligned} \tag{1}$$

where $\mathbf{u} \in \Re^3 = (u, v, w)$ is the nondimensional velocity field and p is the dimensionless pressure. Re is the Reynolds number defined as $Re = U_\infty L/\nu$, where U_∞ is a characteristic velocity, L's a characteristic length, and ν is the kinematic viscosity.

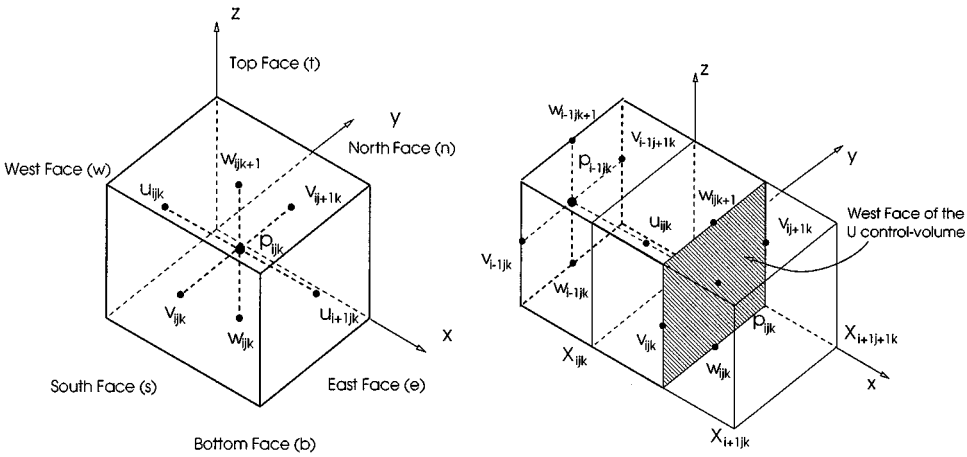

FIG. 1. Placement of the unknowns in the CV (left-hand chart). Control volume where the u-momentum equation is integrated (right-hand chart).

2.1. Discretization

In order to obtain the discrete expression of the nonlinear system, the solution domain is divided into a finite set of control volumes (CVs). In the present work we will use an orthogonally structured grid where each control volume will be hexahedron, as in the left-hand chart in Fig. 1. The variables are stored in a staggered way; i.e., the velocities are evaluated in the faces of the CV and the pressure field at the center of each CV. Staggered discretization has the benefits of stability properties and leads to a natural discrete form of the continuity equation [5, 7].

The procedure carried out to discretize the u-momentum equation will now be described with some detail. In a staggered arrangement of unknowns each equation is integrated in its own CV. The u-momentum CV is built surrounding the u_{ijk} variable, displaced from the CV of the continuity equation, as in the right-hand chart in Fig. 1. In the following, we will refer to the dimensions of this CV Ω as ΔX, ΔY, ΔZ. So we can write the u-momentum equation for a generic node u_{ijk} in its integral form in Cartesian coordinates as

$$\int_\Omega \mathbf{u} \cdot \nabla u \, dV = -\int_\Omega \frac{\partial p}{\partial x} \, dV + \frac{1}{Re} \int_\Omega \Delta u \, dV. \tag{2}$$

The convective term in the momentum equation using the Gauss theorem is rewritten as

$$\int_\Omega \mathbf{u} \cdot \nabla u \, dV = \int_{\partial\Omega} u(\mathbf{u} \cdot \mathbf{n}) \, dS = \sum_k \int_{\partial\Omega_k} u(\mathbf{u} \cdot \mathbf{n}) \, dS, \qquad k = e, w, s, n, t, b, \tag{3}$$

where the indexes $e, w, \ldots$ stand for the standard cardinal notation (see [5]).

The last integral in Eq. (3) is easily approximated applying the midpoint rule. Providing the value of the function in the middle of the face results in the leading truncation term being $\mathcal{O}(h^2)$. Thus, to preserve this accuracy the interpolation of the fluxes at the CV faces has to be at least of second order. This is assured by using a parabolic interpolation for the velocities and linear interpolation for the mass fluxes. Moreover, for nonuniform grids the fluxes are not computed at the middle of the CV. So, assuming a stretched geometric grid

of the form $h_{k+1} = \beta h_k$ with β as the grid-stretching factor, the integral approximation will have a truncation error $\mathcal{O}((\beta - 1)h) + \mathcal{O}(h^2)$. Taking these considerations into account the integral in Eq. (3) is written as

$$\sum_k \int_{\partial\Omega_k} u(\mathbf{u}\cdot\mathbf{n})\, dS \approx \sum_k m_k u_k, \qquad k = e, w, s, n, t, b, \tag{4}$$

where the mass fluxes m_k have been defined as $\int_{\partial\Omega_k} \mathbf{u}\cdot\mathbf{n}\, dS$ and can be evaluated with the expressions

$$\begin{aligned}
m_w &= \frac{u_{ijk} + u_{i-1jk}}{2}\Delta Y \Delta Z, & m_e &= \frac{u_{ijk} + u_{i+1jk}}{2}\Delta Y \Delta Z,\\
m_s &= \frac{v_{ijk}\Delta x_i + v_{i-1jk}\Delta x_{i+1}}{2}\Delta Z, & m_n &= \frac{v_{ij+1k}\Delta x_i + v_{i-1j+1k}\Delta x_{i+1}}{2}\Delta Z,\\
m_b &= \frac{w_{ijk}\Delta x_i + w_{i-1jk}\Delta x_{i+1}}{2}\Delta Y, & m_t &= \frac{w_{ijk+1}\Delta x_i + w_{i-1jk+1}\Delta x_{i+1}}{2}\Delta Y,
\end{aligned}$$

with $\Delta x_{i+1} = x_{i+1jk} - x_{ijk}$ and $\Delta x_i = x_{ijk} - x_{i-1jk}$ (see Fig. 1). The velocity at the CV face is interpolated by fitting a parabola to the values of the velocity at three consecutive nodes: the two nodes located on either side of the surface of interest plus the adjacent node in the upstream direction. In this work we will use the QUICK formulation of Hayase *et al.* [6], which can be seen as a defect-correction scheme based on the upwind difference approximation:

$$\begin{aligned}
u_e &= \begin{cases} u_{ijk} + S_e^+ \ (\mathbf{u}\cdot\mathbf{n})_e > 0, \\ u_{i+1jk} + S_e^- \ (\mathbf{u}\cdot\mathbf{n})_e < 0, \end{cases} & u_w &= \begin{cases} u_{ijk} + S_w^+ \ (\mathbf{u}\cdot\mathbf{n})_w > 0, \\ u_{i-1jk} + S_w^- \ (\mathbf{u}\cdot\mathbf{n})_w < 0, \end{cases}\\
u_n &= \begin{cases} u_{ijk} + S_n^+ \ (\mathbf{u}\cdot\mathbf{n})_n > 0, \\ u_{ij+1k} + S_n^- \ (\mathbf{u}\cdot\mathbf{n})_n < 0, \end{cases} & u_s &= \begin{cases} u_{ijk} + S_s^+ \ (\mathbf{u}\cdot\mathbf{n})_s > 0, \\ u_{ij-1k} + S_s^- \ (\mathbf{u}\cdot\mathbf{n})_s < 0, \end{cases}\\
u_t &= \begin{cases} u_{ijk} + S_t^+ \ (\mathbf{u}\cdot\mathbf{n})_t > 0, \\ u_{ijk+1} + S_t^- \ (\mathbf{u}\cdot\mathbf{n})_t < 0, \end{cases} & u_b &= \begin{cases} u_{ijk} + S_b^+ \ (\mathbf{u}\cdot\mathbf{n})_b > 0, \\ u_{ijk-1} + S_b^- \ (\mathbf{u}\cdot\mathbf{n})_b < 0. \end{cases}
\end{aligned}$$

The defect-correction source terms S^+ and S^- are calculated within the multigrid cycle using the current approximation whenever a discrete evaluation of the residual is needed. So the algebraic coefficients for the convection terms can be written as

$$\begin{aligned}
L_e^c = \min(0, m_e), \quad L_w^c = \min(0, m_w), \quad L_n^c = \min(0, m_n),\\
L_s^c = \min(0, m_s), \quad L_t^c = \min(0, m_t), \quad L_b^c = \min(0, m_b),\\
L_p^c = -\left(L_e^c + L_n^c + L_s^c + L_b^c + L_t^c + L_w^c\right).
\end{aligned} \tag{5}$$

The expression for L_p^c has been obtained using the continuity equation over the CV Ω, which in its discrete form is

$$m_e + m_w + m_n + m_s + m_t + m_b = 0.$$

Using the Gauss theorem in the diffusive part of the momentum equation (3) and the midpoint rule to approximate the resulting surface integral we get

$$\int_{\partial\Omega} \nabla u \cdot \mathbf{n}\, dS \approx \left[\left(\frac{\partial u}{\partial x}\right)_e - \left(\frac{\partial u}{\partial x}\right)_w\right] \Delta S_x + \left[\left(\frac{\partial u}{\partial y}\right)_n - \left(\frac{\partial u}{\partial y}\right)_s\right] \Delta S_y + \left[\left(\frac{\partial u}{\partial z}\right)_t - \left(\frac{\partial u}{\partial z}\right)_b\right] \Delta S_z. \quad (6)$$

The derivatives in the above expression are evaluated with a central difference scheme:

$$L_e^d = \frac{\Delta Y \Delta Z}{Re(x_{i+1jk} - x_{ijk})}, \quad L_w^d = \frac{\Delta Y \Delta Z}{Re(x_{ijk} - x_{i-1jk})}, \quad L_n^d = \frac{2\Delta X \Delta Z}{Re(y_{ij+1k} - y_{ij-1k})},$$
$$L_s^d = \frac{2\Delta X \Delta Z}{Re(y_{ij+2k} - y_{ijk})}, \quad L_t^d = \frac{2\Delta Y \Delta X}{Re(z_{ijk+1} - z_{ijk-1})}, \quad L_b^d = \frac{2\Delta Y \Delta X}{Re(z_{ijk+2} - z_{ijk})}, \quad (7)$$
$$L_p^d = -\left(L_e^d + L_n^d + L_s^d + L_b^d + L_t^d + L_w^d\right).$$

Finally, treating the pressure as a surface force the volume integral in Eq. (2) can be expressed as a surface integral, as in Eq. (8). Again this is evaluated using the midpoint rule approximation,

$$-\int_{\partial\Omega} p\,\mathbf{i} \cdot \mathbf{n}\, dS \approx (p_w - p_e)\, \Delta S_x \quad \mathbf{i} = (1, 0, 0). \quad (8)$$

In this case no interpolation is needed for the pressure because of the staggered arrangements of unknowns, as can be seen in the right-hand chart in Fig. 1. Now, we can write the algebraic equation for a generic velocity node u_{ijk} as

$$L_w^u u_{i-1jk} + L_e^u u_{i+1jk} + L_s^u u_{ij-1k} + L_n^u u_{ij+1k} + L_b^u u_{ijk-1} + L_t^u u_{ijk+1} + L_p^u u_{ijk} + L_p^p p_{ijk} + L_w^p p_{i-1jk} = F_{ijk}. \quad (9)$$

The coefficients multiplying the velocity u are obtained as the sum of the diffusive and convective parts, (i.e., $L_l^u = L_l^c + L_l^d$ with $l = e, w, n, s, b, t$) and those multiplying the pressure are obtained directly from Eq. (8). An equivalent expression may be obtained for the v- and w-momentum equations and can be derived by symmetry from the above equations.

The continuity equation can be easily approximated because all velocities are known within the surface of the volume:

$$\int_\Omega \nabla \cdot \mathbf{u}\, dV \approx (u_e - u_w)\Delta Y \Delta Z + (v_n - v_s)\Delta X \Delta Z + (w_t - w_b)\Delta X \Delta Y. \quad (10)$$

The above expressions are valid for CVs inside the domain and must be modified in order to satisfy the conditions. The discretization of the boundary conditions is performed by mirroring the cells adjacent to the boundary. The new variables outside the solution domain are extrapolated invoking the condition at each boundary. With these modifications

of the algebraic equations the system of nonlinear equations to be solved can be presented in a matrix form as

$$\begin{pmatrix} L_u^h & 0 & 0 & L_p^h \\ 0 & L_v^h & 0 & L_p^h \\ 0 & 0 & L_w^h & L_p^h \\ L_m^h & L_m^h & L_m^h & 0 \end{pmatrix} \begin{pmatrix} u \\ v \\ w \\ p \end{pmatrix} = \begin{pmatrix} f_u \\ f_v \\ f_w \\ f_p \end{pmatrix}, \tag{11}$$

where the source terms f_u, f_v, f_w, and f_p in the right-hand side of the system include the discretization of the boundary conditions and the contribution of the QUICK scheme.

3. THE MULTIGRID METHOD

A sequence of grids $\Omega^l (l = 1, \ldots, M)$ is used in the full multigrid (FMG) scheme [1] where Ω^1 is the finest target grid and the rest of the grids are obtained by applying cell-centered coarsening. The computations are initiated in the coarsest grid; once the discrete system is solved the solution is transferred to the next finer level. The prolongated solution is then used as an initial guess for the multigrid method in that level. This procedure is repeated until the finest grid is reached. The goal of this algorithm is to reduce the algebraic error to below the discretization error in just one FMG cycle.

Because of the nonlinearity of the problem, a full approximation scheme (FAS) [1] is used to solve each level in the FMG cycle. The following iterative algorithm represents a FAS V(γ_1, γ_2)-cycle to solve the nonlinear system $Lu = f$ on Ω^1 where γ_1 and γ_2 represent the number of pre-smoothing and post-smoothing iterations respectively.

ALGORITHM 1 (FAS V(γ_1, γ_2)).

1. **Pre-smoothing**: Apply γ_1 iterations of the smoothing method to $L^1 u^1 = f^1$
2. **FOR** l = 1 **TO** L Restriction Part
3. Compute the residual $r^{l-1} = f^{l-1} - L^{l-1} u^{l-1}$
4. Restriction of the residual $r^l = R_{l-1}^l r^{l-1}$
5. Restriction of the solution $u_{old}^l = I_{l-1}^l u^{l-1}$
6. Compute the metrics of level l $L^l(u_{old}^l)$
7. Calculate the new right-hand side $f^l = r^l + L^l u_{old}^l$
8. **Pre-smoothing**: Apply γ_1 iterations of the smoothing method to $L^l u^l = f^l$
9. **FOR** l = $L - 1$ **TO** 1 Prolongation Part
10. Correction of the current approximation $u^l = u^l + P_l^{l+1}(u^{l+1} - u_{old}^{l+1})$
11. Compute the metrics of level l $L^l(u^l)$
12. **Post-smoothing**: Apply γ_2 iterations of the smoothing method to $L^l u^l = f^l$

In steps 6 and 11 the metrics of the system are computed over the current grid, which includes the computation of the correction terms from the QUICK scheme and also the linearization of the system based on the actual solution. Note that the metrics of the system are also updated within the smoothing process in steps 8 and 12 as explained in Section 3.1. The operators R_{l-1}^l and P_l^{l+1} in steps 3 and 8 are used to transfer data (solution and residuals) between two different grids: from the coarser level to the current (prolongation) or from the finer to the current level (restriction), respectively.

These transfer operators are dictated by the staggered arrangement of unknowns and the coarsening procedure used. The prolongation and restriction operators are volume-weighted

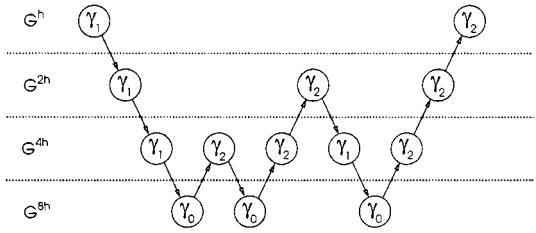

FIG. 2. Scheme of an F-cycle F(γ_1,γ_2) where γ_0 represents the number of iterations of the smoother performed to solve the coarsest level.

trilinear interpolation in the case of standard coarsening. For the semi-coarsening approach the velocity component parallel to the coarsened direction is restricted using injection; the other variables are restricted using volume-weighted linear interpolation in lines parallel to the coarsened direction. The prolongation operator in this case is volume-weighted linear interpolation. Note that for semi-coarsening the velocity component parallel to the coarsened direction is treated in a vertex-centered way, while the rest of the variables are transferred as cell centered.

In the following experiments F-cycles will be used (see Fig. 2) to solve each level of the FMG algorithm. F-cycles have been reported to be more efficient for rotating problems [17] at the expense of their parallel properties [10]. The coarsest level is fixed as coarse as possible, and it will be solved with five iterations of the smoothing process.

3.1. Smoothing Process

One of the most important parts of a multigrid algorithm is the smoothing process. Several smoothers for the Navier–Stokes equations problem were studied in the literature. These approaches fall into two categories: 1. coupled smoothing [23, 16, 22] where the momentum and continuity equations are satisfied simultaneously), and 2. distributive smoothing [21, 3] (where the momentum equations are solved in a first step, and then the velocities and pressures are corrected in order to satisfy the continuity equation). In situations where the coefficients vary through the CV (e.g., stretched grids, strong recirculating flows, . . .)coupled smoothing has advantages over the distributive approach because the linearized momentum and continuity equations are solved simultaneously [23, 7]. However, the computational cost of the coupled method is much higher than that of the distributive. Note that a (small) matrix has to be inverted in each CV. Moreover, every velocity component is updated essentially twice since it updates all the variables involved in a CV simultaneously (see the right-hand chart in Fig. 1).

In particular, we have chosen a cell-implicit symmetric coupled Gauss-Seidel (SCGS) method as the base smoother because of its higher stability and rapid convergence. This smoother was introduced by Vanka [23] and also considered by Thompson and Tenziger [22]. Considering the CV ijk, the momentum equations for the six cell faces together with the continuity equation for the CV can be expressed as

$$\sum_{|m|+|n|+|p|\le 1} L^{u_w}_{i+m,j+n,k+p} u_{i+m,j+n,k+p} + L^{u_w}_{p_i} p_{ijk} + L^{u_w}_{p_{i-1}} p_{i-1jk} = f^u_{ijk},$$

$$\sum_{|m|+|n|+|p|\le 1} L^{u_e}_{i+m,j+n,k+p} u_{i+m,j+n,k+p} + L^{u_e}_{p_i} p_{i+1jk} + L^{u_e}_{p_{i-1}} p_{ijk} = f^u_{i+1jk},$$

$$
\begin{aligned}
\sum_{|m|+|n|+|p|\le 1} L^{v_s}_{i+m,j+n,k+p} v_{i+m,j+n,k+p} + L^{v_s}_{p_j} p_{ijk} + L^{u_v}_{p_{j-1}} p_{ij-1k} &= f^v_{ijk},\\
\sum_{|m|+|n|+|p|\le 1} L^{v_n}_{i+m,j+n,k+p} v_{i+m,j+n,k+p} + L^{v_n}_{p_j} p_{ij+1k} + L^{v_n}_{p_{j-1}} p_{ijk} &= f^v_{ij+1k},\\
\sum_{|m|+|n|+|p|\le 1} L^{w_b}_{i+m,j+n,k+p} w_{i+m,j+n,k+p} + L^{w_b}_{p_k} p_{ijk} + L^{w_b}_{p_{k-1}} p_{ijk-1} &= f^w_{ijk},\\
\sum_{|m|+|n|+|p|\le 1} L^{w_t}_{i+m,j+n,k+p} w_{i+m,j+n,k+p} + L^{w_t}_{p_k} p_{ijk+1} + L^{w_t}_{p_{k-1}} p_{ijk} &= f^w_{ijk+1},\\
\frac{(u_{i+1jk}-u_{ijk})}{\Delta X} + \frac{(v_{ij+1k}-v_{ijk})}{\Delta y} + \frac{(w_{ijk+1}-w_{ijk})}{\Delta Z} &= f^m_{ijk}.
\end{aligned}
\tag{12}
$$

This set of equations for the CV is linearized by computing the mass fluxes, $L^{u,v,w}$, with the current values of the velocity field. Defining the residuals $r^{u,v,w}$ and the corrections $\Delta u = u^{n+1} - u^n$, etc. the system (12) can be arranged in a block structure as follows:

$$
\begin{pmatrix}
L^{uw}_{ijk} & 0 & 0 & 0 & 0 & 0 & L^{u_w}_{p_i}\\
0 & L^{ue}_{i+1jk} & 0 & 0 & 0 & 0 & L^{u_e}_{p_{i-1}}\\
0 & 0 & L^{vs}_{ijk} & 0 & 0 & 0 & L^{v_s}_{p_j}\\
0 & 0 & 0 & L^{vn}_{ij+1k} & 0 & 0 & L^{v_n}_{p_{j-1}}\\
0 & 0 & 0 & 0 & L^{wb}_{ijk} & 0 & L^{w_b}_{p_k}\\
0 & 0 & 0 & 0 & 0 & L^{wt}_{ijk+1} & L^{w_t}_{p_{k-1}}\\
-\frac{1}{\Delta X} & \frac{1}{\Delta X} & -\frac{1}{\Delta Y} & \frac{1}{\Delta Y} & -\frac{1}{\Delta Z} & \frac{1}{\Delta Z} & 0
\end{pmatrix}
\begin{pmatrix}
\Delta u_{ijk}\\ \Delta u_{i+1jk}\\ \Delta v_{ijk}\\ \Delta v_{ij+1k}\\ \Delta w_{ijk}\\ \Delta w_{ijk+1}\\ \Delta p_{ijk}
\end{pmatrix}
=
\begin{pmatrix}
r^u_{ijk}\\ r^u_{i+1jk}\\ r^v_{ijk}\\ r^v_{ij+1k}\\ r^w_{ijk}\\ r^w_{ijk+1}\\ r^m_{ijk}
\end{pmatrix}.
\tag{13}
$$

A more implicit version of Eqs. (13) that includes off-diagonal elements in the first six rows is also possible; this is equivalent to considering implicitly in the Eqs. (12) all the unknowns involved in the CV. However, the convergence factor is similar and the system is more expensive to solve than the system of Eqs. (13) [22]. The system (13) is easily solved by Gaussian elimination and then the velocity components and the pressure of the CV are updated using underrelaxation:

$$
\begin{aligned}
\mathbf{u}^{n+1} &= \mathbf{u}^n + \omega_u \Delta \mathbf{u},\\
p^{n+1} &= p^n + \omega_p \Delta p.
\end{aligned}
\tag{14}
$$

The underrelaxation technique has the effect of adding a pseudo–time dependent term in the equations. In the following simulations the underrelaxation factor for the pressure, ω_p, has been fixed to 1.0, while the underrelaxation factor for the velocities, ω_u, is strongly problem dependent and has to be set empirically. The optimum value of ω_u is a function of the Reynolds number and the grid size and also depends on whether the convection scheme is first- (upwind) or second-order (QUICK) accurate. This is a drawback of this smoother, since a simulation has to be tuned in order to find out the best underrelaxation factor. As Fig. 3 shows, the efficiency of the method can be dramatically worsened with a bad choice of ω_u.

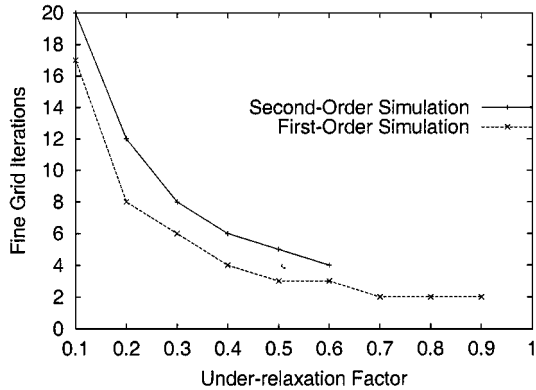

FIG. 3. Number of fine-grid cycles required to converge a driven-cavity simulation with $Re = 500$ on a $16 \times 16 \times 16$ uniform grid as a function of the relaxation parameter ω_u.

3.2. Plane-Implicit Smoothers

Implicit solvers have been widely considered in previous work as a cure to eliminating all the high-frequency errors in the presence of strong anisotropies. Taking advantage of the relatively small 1-D problem size, these implicit-line smoothers are based on an exact solver. However, the 3-D counterpart does not present this possibility, since the 2-D problem size is no longer small enough for us to consider using an exact solver. Furthermore a direct exact solver for the planes is not needed, as has been shown in [8] for the 3-D Poisson equation and in [16] for the incompressible Navier–Stokes equations. This consideration drastically reduces the computational cost of the overall algorithm compared with that of an exact plane solver. However, this inexact solution of the planes does not decrease the convergence of the multigrid algorithm [16, 8]; in other words, solving the plane beyond a precision threshold does not improve the convergence rate. Note that the plane-implicit smoother has to damp high oscillating error components in the plane rather than solve a 2-D problem exactly.

In the present work, the planes will be approximately solved with a 2-D multigrid algorithm consisting of one FAS F(1,1)-cycle. The same kind of anisotropies found in the 3-D problem may appear in the 2-D system. Thus a robust multigrid algorithm is, again, completely necessary. For the 2-D system the same robust algorithms will be considered, i.e., an alternating-line smoother combined with full coarsening and a line-implicit smoother combined with semi-coarsening. In the following simulations, the 2-D algorithm used to solve the planes will be the 3-D counterpart, i.e., an alternating-line smoother when using an alternating-plane smoother and a semi-coarsened line smoother when using a semi-coarsened plane smoother. One 1-D FAS F(1, 1)-cycle will be applied to solve the lines, the smoother in this case being SCGS as described in the previous section.

The coupled philosophy of the SCGS will be applied in the line and plane solvers. The plane smoother relaxes simultaneously the momentum and continuity equations of the cells included in the plane, and hence all velocity components and pressures contained within the plane will be updated at the same time. Let us consider for example an xy plane, defining the vector X_k that accommodates the variables for a whole plane of cells:

$$X_k^T = (\mathbf{u}, \mathbf{v}, \mathbf{w}, \mathbf{w}^+, \mathbf{p}), \quad \mathbf{u} = u_{ijk}, \quad \mathbf{v} = v_{ijk}, \quad \mathbf{w} = w_{ijk}, \quad \mathbf{w}^+ = w_{ijk+1},$$
$$\mathbf{p} = p_{ijk}, \forall i,\ j \in [0, n], \quad k = const. \tag{14}$$

The equation system for the plane in terms of residuals and corrections is

$$L_k \, \Delta X_k = R_k, \tag{15}$$

where $R_k = f_k - L_k X_k$ is the residual of the kth plane and $\Delta X_k = X_k^{n+1} - X_k^n$ is the increment of the solution. The system of equations (15) is built into the smoothing process as follows. When solving for the kth plane, the metrics in that plane are linearized using the current solution. Also the second-order correction for the convective term is recomputed. With these new metrics the residual R_k for the kth plane is calculated.

Defining a specific ordering of the planes, we can easily construct many types of plane smoothers. It is important to note that with the second-order operator, the right-hand side of the system (15) depends on the values of the plane k, $k \pm 1$ and/or $k \pm 2$, depending on the direction of the velocity. Thus a parallel implementation cannot be constructed based on a regular zebra ordering (left-hand chart in Fig. 4). In order to avoid these dependencies a tri-plane smoother could be applied [17] (right-hand chart in Fig. 4).

Grid stretching is commonly used in grid generation to pack points into regions with large solution gradients while avoiding an excess of points in more benign regions (for example in the simulation of viscous flows at high Reynolds numbers to resolve boundary layers). The convergence of multigrid based on point smoothing and full coarsening deteriorates dramatically when highly stretched grids are used. In some situations, when the direction of the anisotropies is known beforehand, the multigrid convergence can be improved using an implicit smoother in the direction normal to the stretching. However, if the stretched grid generates aspect ratios whose relative magnitudes vary for different parts of the computational domain, the multigrid techniques based on plane-wise smoothers combined with full coarsening fail to smooth error components. Other remedies should be used to achieve a robust solver. The two most common alternatives are:

Robust multigrid smoothing process with standard coarsening. If the coarser grids are built by doubling the mesh size in all coordinate directions, sweeps of the planes in

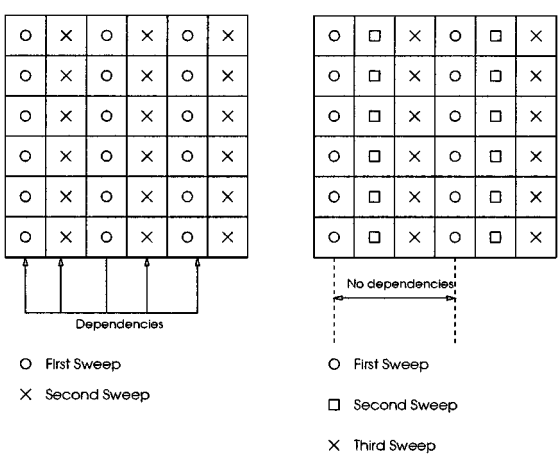

FIG. 4. Standard zebra ordering of planes (left-hand chart). Planes relaxed concurrently in a tri-plane smoother (right-hand chart).

the three directions are needed to achieve robustness (yz-plane smoothing sweep $\rightarrow$ xz-plane smoothing sweep $\rightarrow$ xy-plane smoothing sweep). From here on, this approach will be referred to as *alternating-plane smoothers* (APS). Several versions of this method can be developed depending on the sweep ordering (see [24] for a definition of the several orderings mentioned next): symmetric alternating-plane smoother (S-APS), lexicographic alternating-plane smoother (L-APS), and tri-plane alternating-plane smoother (Tri-APS).

Plane-implicit smoothers combined with semi-coarsening. Instead of using standard coarsening the coarse levels can be built by only coarsening along one direction. In order to achieve robustness a plane-implicit solver perpendicular to the coarsened direction is needed. Based on the coarsened direction, we will refer to these approaches as X, Y, or Z semi-coarsening (XSC, YSC, ZSC). Depending on the order in which the planes are swept we can construct the following methods: symmetric Z semi-coarsening (S-ZSC), lexicographic Z semi-coarsening (L-ZSC), and tri-plane Z semi-coarsening (Tri-ZSC).

4. NUMERICAL EXPERIMENTS

Two different flows have been chosen to test the robustness of the multigrid algorithms described: the driven cavity and the flow over a flat plate. These two cases have been widely studied and used as benchmarking problems for CFD codes. Although the flow structures are relatively simple, they exhibit some basic problems that prevent optimal multigrid efficiencies from being achieved [2], namely strong recirculating flows and boundary layers.

Let R be the L_2-norm of the average residual of the system of equations (11) defined as

$$R = \left(\frac{\sum \left(\left(R^u_{ijk}\right)^2 + \left(R^v_{ijk}\right)^2 + \left(R^w_{ijk}\right)^2 + \left(R^c_{ijk}\right)^2 \right)}{4 \cdot N_x \cdot N_y \cdot N_z} \right)^{\frac{1}{2}}, \tag{16}$$

where R^u, R^v, R^w, R^c are the residuals of the u-, v-, w-momentum equations and continuity equation respectively. The convergence criterion is based on R. When the fine-grid average residual decreases to below 10^{-4} the calculations are terminated. This value is small enough to assure that the algebraic error is below the discretization error. Let R_0 and R_n denote respectively the residual norms (as defined in Eq. (16)) before the iterative process and after the convergence criterion is satisfied. So the average convergence factor is defined by

$$\bar{\varrho} = \left(\frac{R_n}{R_0} \right)^{\frac{1}{n}}. \tag{17}$$

4.1. Flow in a Driven Cavity

The numerical solution, which has been widely used for testing numerical schemes, is that of a flow confined in a rectangular domain with the upper wall moving at a constant speed. The flow structure for *low to moderate* Reynolds numbers consists of a 3-D primary vortex and two 3-D secondary vortexes at the bottom (see Fig. 5). The problem currently considered consists of a cube of dimension L with the top wall ($z = L$) moving at a velocity u. The Reynolds number of the flow based in these quantities is $Re = uL/\nu$. The boundary conditions are of Dirichlet type for the velocities on the six faces of the computational domain, and no boundary conditions were necessary for the pressure.

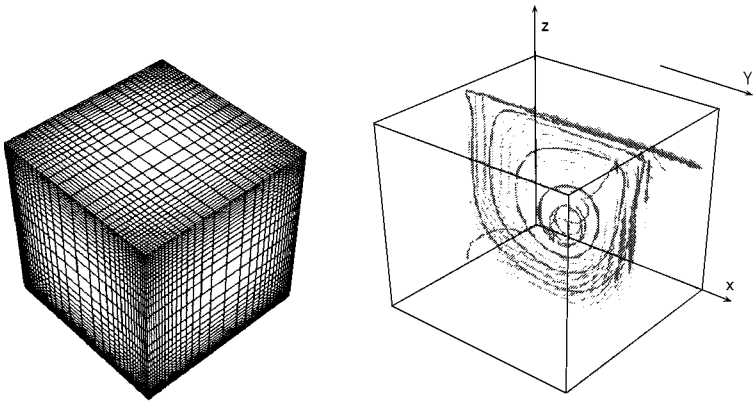

FIG. 5. Grid used for the driven-cavity problem $32 \times 32 \times 32$ (left-hand chart) and structure of the 3-D primary vortex for $Re = 10^3$ (right-hand chart).

Simulations have been performed over three different grids, each one uniform and stretched: $16 \times 16 \times 16$, $32 \times 32 \times 32$, and $64 \times 64 \times 64$. The stretched grids were of the form $h_{k+1} = \beta h_k$, the stretching factor β being equal to 1.1 in all cases (see Fig. 5, left-hand chart). The driven-cavity problem is a rotating flow for which standard multigrid schemes might have difficulties converging. These difficulties were not experienced in this work since a moderate Reynolds number was considered. However, the simulations result in a complex recirculating flow consisting of 3-D vortex structures as can be seen in Fig. 5. The profiles at the center line of the cavity with $Re = 3200$ on a $32 \times 32 \times 32$ stretched grid are compared with the experiment of Prasad and Koseff [18] in Fig. 6.

As mentioned in Section 3.1, the convergence factor varies with the choice of the underrelaxation factor for the velocity field. In Table I the underrelaxation factors used in each simulation, as a function of the Reynolds number and grid size, are shown for the different multigrid cycles under study: SCGS, tri-plane and symmetric APS, and tri-plane and symmetric ZSC.

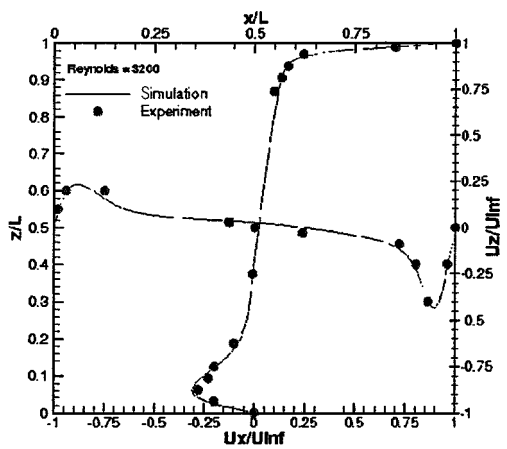

FIG. 6. 3-D cavity central plane profiles for $Re = 3200$ over a $32 \times 32 \times 32$ stretched grid compared with experiment [18].

TABLE I
Underrelaxation Factors for the Driven-Cavity Simulation as a Function of the Grid Size, Reynolds Number, and Multigrid Cycle

	Grid								
	$16 \times 16 \times 16$			$32 \times 32 \times 32$			$64 \times 64 \times 64$		
Re	SCGS	APS	ZSC	SCGS	APS	ZSC	SCGS	APS	ZSC
10^2	0.6	0.6	0.5	0.5	0.6	0.6	0.5	0.6	0.5
10^3	0.4	0.3	0.4	0.3	0.3	0.3	0.3	0.3	0.3

Figure 7 shows the L_2-norm of the residual versus F(1,1)-cycles with a SCGS smoother for several uniform grids and Reynolds numbers. The behavior of this smoother is quite good for low Reynolds numbers (left-hand graph in Fig. 7 for Reynolds number 10^2), with the residual norm being reduced by between four and five orders of magnitude in the first five cycles. However, its efficiency decreases as the problem becomes more convective. The residual norm cannot be reduced by four orders of magnitude in 10 cycles (right-hand graph in Fig. 7 for Reynolds number 10^3). Furthermore, convergence could not be attained over stretched grids with a cell-wise smoother such as SCGS.

Figure 8 shows the L_2-norm of the residual versus F(1,1)-cycles with an alternating-plane smoother combined with full coarsening (APS) for several grids and Reynolds numbers. The S-APS approach (top graphs in Fig. 8) converges the residual to below 10^{-4} in five cycles for both Reynolds numbers (10^2 and 10^3). However, the Tri-APS approach (bottom graphs in Fig. 8) need eight cycles to reduce the residual norm to below 10^{-4} for Reynolds number 10^3. It is interesting to note that the cost per multigrid cycle with the symmetric ordering is about twice as large as that with the tri-plane ordering. However, convergence factor per work unit is better with the symmetric ordering of planes for low Reynolds numbers and it is similar for both smoothers for $Re = 10^3$.

One of the drawbacks of the APS approach is its difficult implementation in a parallel setting [13]. This problem can be easily overcome using a plane smoother combined with semi-coarsening to ensure robustness. The block-implicit smoother used to converge the driven-cavity simulation needs to be applied along the subcharacteristics of the discrete

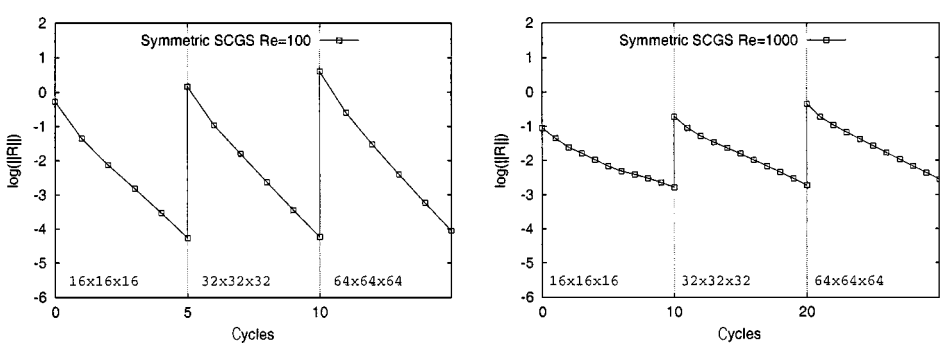

FIG. 7. L_2-norm of the residual versus F(1,1)-cycles with SCGS smoother for several uniform grids and Reynolds numbers for the driven-cavity simulation.

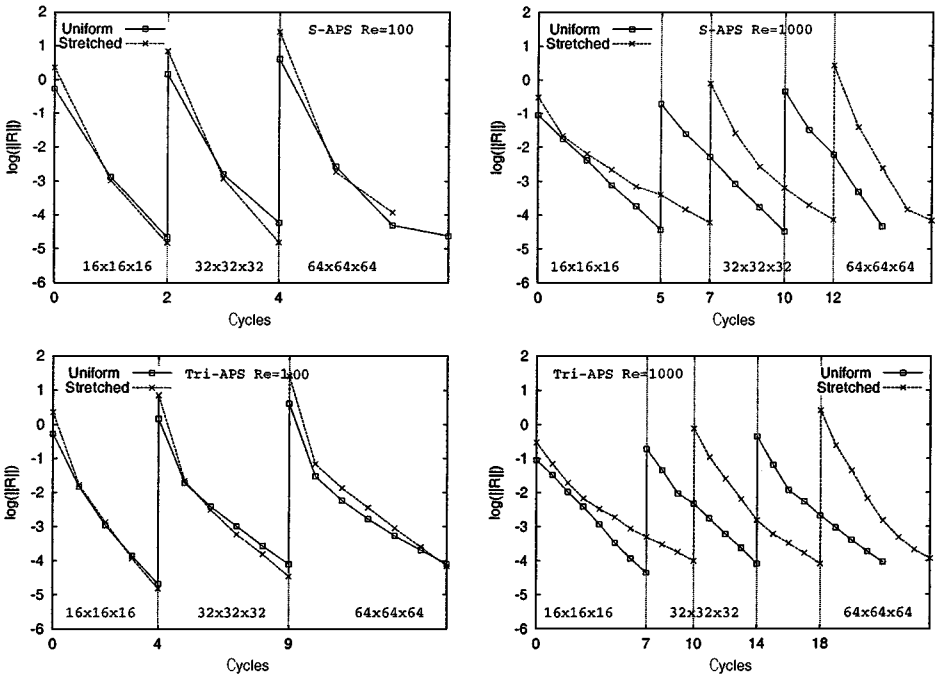

FIG. 8. L_2-norm of the residual versus F(1,1)-cycles with an alternating-plane smoother combined with full coarsening (APS) for several grids and Reynolds numbers with a symmetric order of planes (top graphs) and a tri-plane ordering (low graphs) for the driven-cavity simulation.

operator for convection-dominated problems in order to obtain the higher efficiency. For example, it was observed that the xz-plane sweeps seriously harm the smoothing, and so the YSC approach exhibits a poor behavior.

Figure 9 shows the L_2-norm of the residual versus F(1,1)-cycles with an xy-plane implicit smoother combined with ZSC for several grids and Reynolds numbers. Although not shown, the behavior exhibited by the XSC approach is similar to the one presented in Fig. 9 for ZSC. The S-ZSC approach (top graphs in Fig. 9) converges the residuals to below 10^{-4} in five cycles for both Reynolds numbers (10^2 and 10^3). However, the Tri-ZSC approach (bottom-charts in Fig. 9) is unable to reduce the residual norm below 10^{-4} in 10 cycles for Reynolds number 10^3. As one might expect, the time per cycle is twice as fast for the tri-plane ordering, although the convergence factor per work unit is better with the symmetric ordering for all the cases.

Table II shows the average convergence factors obtained in the simulation of the driven-cavity problem for several uniform and stretched grids, Reynolds numbers, and F(1,1)-cycles. The convergence factor has been proved to be independent of the grid size and stretching for the two robust approaches investigated; however, the convergence is not Reynolds number–independent for the driven-cavity simulation. The algorithms exhibit the same behavior for low Reynolds numbers as when solving the Poisson equation; that is, the residual reduction per cycle is similar in both situations [8]. The convergence factor improves on stretched grids (as in the fully elliptic case [8]), and as shown in Table II. It also improves for finer grids. The convergence factor for the APS approach is lower than for the SC approach and its cost per cycle is have as much because the F-cycle spends a lot of time on coarser levels. However, its difficult and low-efficiency parallelization and

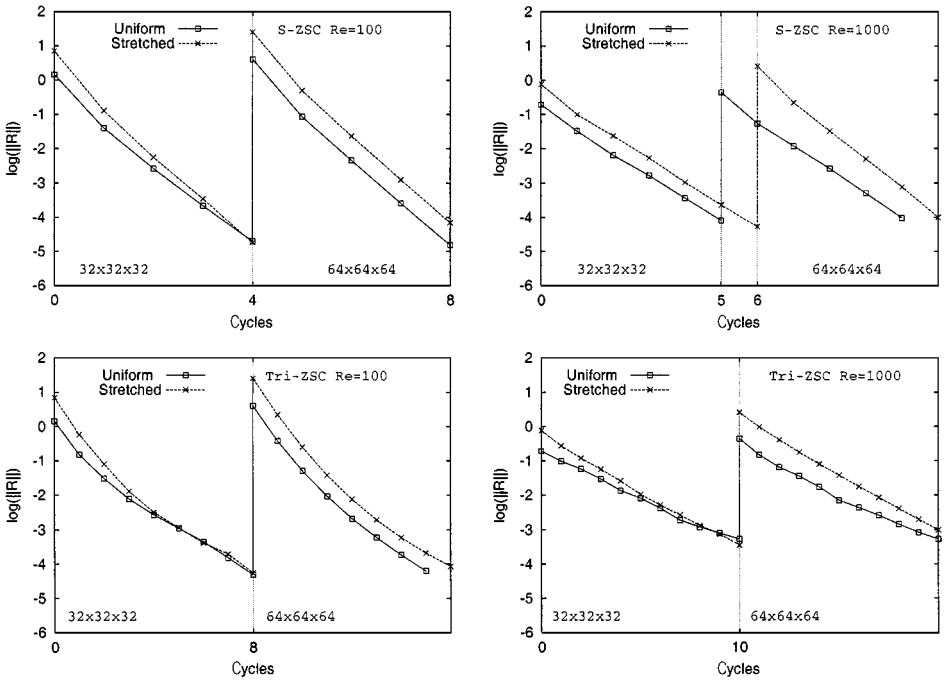

FIG. 9. L_2-norm of the average residual versus F(1,1)-cycles with an xy-plane implicit smoother combined with ZSC for several grids and Reynolds numbers with a symmetric order of planes (top graphs) and a tri-plane ordering (low graphs) for the driven-cavity simulation.

its difficulty in converging for Reynolds numbers higher than 10^3 might make the semi-coarsening approach more attractive.

4.2. 3-D Flat-Plate Boundary Layer

We consider a square plate placed in the middle of the solution domain. In the west face ($x = 0$) we define the inflow boundary with no angle of attack, and so the east face will hold the outflow condition. On the plate a no-slip boundary condition is imposed, and a symmetric condition is imposed elsewhere on the domain boundary (see left-hand chart in

TABLE II

Average Convergence Factors Obtained in the Simulation of the Driven-Cavity Problem for Several Uniform (U) and Stretched (S) Grids, Reynolds Numbers, and Different F(1,1), Cycles

	Grid							
	$32 \times 32 \times 32$				$64 \times 64 \times 64$			
Re	S-APS	S-ZSC	Tri-APS	Tri-ZSC	S-APS	S-ZSC	Tri-APS	Tri-ZSC
10^2 U	1.6×10^{-3}	0.07	0.14	0.24	3×10^{-3}	0.04	0.17	0.21
10^2 S	1.4×10^{-3}	0.04	0.08	0.23	7×10^{-3}	0.04	0.07	0.2
10^3 U	0.17	0.21	0.25	0.5	0.1	0.18	0.34	0.5
10^3 S	0.15	0.21	0.3	0.46	0.1	0.15	0.34	0.46

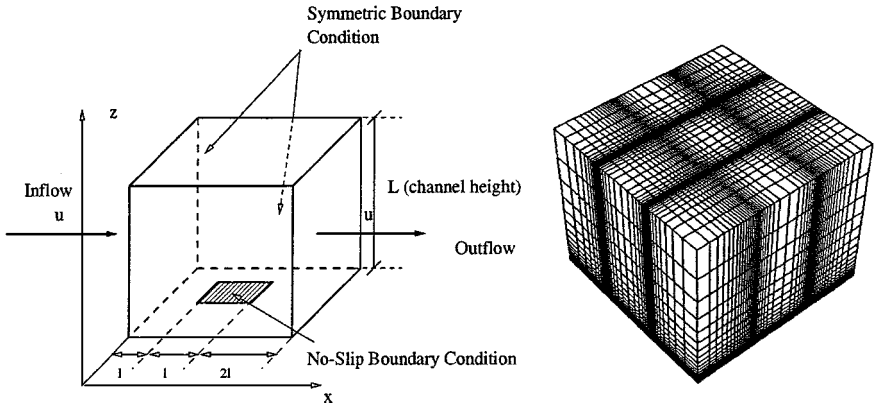

FIG. 10. Schematic configuration of the flat-plate simulation (left-hand chart). $48 \times 48 \times 64$ grid used for the flat-plate simulation (right-hand chart).

Fig. 10). In this case, the pressure is not specified at the boundary. As the velocity gradient normal to the wall is very high only in the boundary layer, the thin-layer approximation which only retains those terms can be adopted. However, in the following simulations the original for (1) of the Navier–Stokes equations is solved.

In order to capture the viscous effects, the grid is highly stretched near the plate (see right-hand chart in Fig. 10). Moreover, the grid is refined near the plate edges to reduce the large discretization errors in those zones, as advocated by Thomas *et al.* [21]. To ensure that a sufficient number of grid points will lie inside the boundary layer, the space for a uniform mesh would impose too high a demand on the computation. For example, approximating the boundary-layer thickness with $\delta \sim 1/\sqrt{Re}$ for $Re = 10^4$ we have $\delta \sim 0.01$, which implies at least 10^2 grid points in a uniform grid, which cannot be considered due to memory limitations in a 3-D simulation. Thus for this model problem, no regular grids will be considered. The grids are stretched in the z-direction using a geometric factor $h_k = \beta h_{k-1}$ with $\beta = 1.3$ for the $24 \times 24 \times 32$ grid and $\beta = 1.1$ for the $48 \times 48 \times 64$ grid.

The solution is verified by comparing the u-velocity in the middle of the plate with the Blasius analytical solution for a 2-D plate (left-hand chart in Fig. 11). The little discrepancy near the layer edge is due to the highly stretched grid used in this simulation.

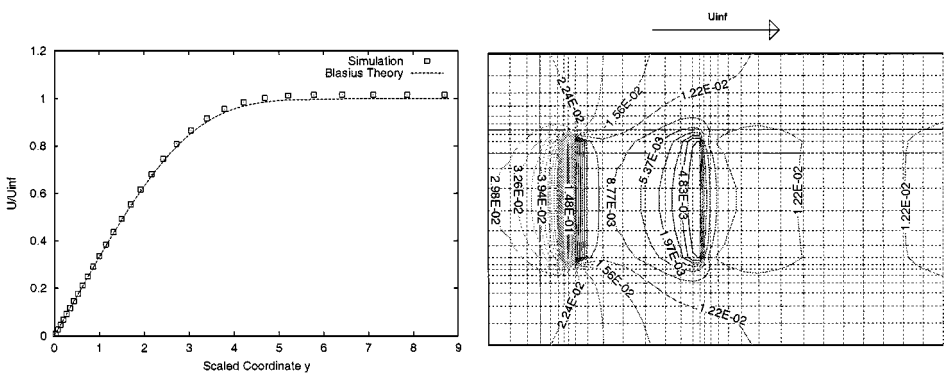

FIG. 11. Simulation comparison with Blasius theory at the middle of the plate with $Re = 10^4$ (left-hand chart). Pressure contour lines for $Re = 10^4$ and $z = 0$ (right-hand chart).

TABLE III
Underrelaxation Factors for the Flat-Plate Simulation as a Function of the Grid Size, Reynolds Number, and Multigrid Cycle

	Grid			
	$24 \times 24 \times 32$		$48 \times 48 \times 64$	
Re	L-ZSC	Tri-ZSC	L-ZSC	Tri-ZSC
10^2	0.8	0.8	0.8	0.8
10^4	0.6	0.4	0.6	0.4

The multigrid cycle employed to solve each level of the FMG is a F(2,1)-cycle. The underrelaxation factors used in the simulations are shown in Table III. Depending on the problem, some plane-sweep directions may deteriorate the smoothing. The best smoothing rate was achieved with a combination of xy-plane relaxation and ZSC. We do not include results of the alternating-plane approach or other semi-coarsening directions because of their poor behavior.

Figure 12 shows the L_2-norm of the residual versus F(2,1)-cycles with lexicographic and tri-plane xy-plane implicit smoothers combined with ZSC for several grids and Reynolds numbers. The residual norm is reduced by nearly five orders of magnitude in the first five cycles in all cases (note that the reduction is of four orders of magnitude in the first two cycles for the $48 \times 48 \times 64$ grid). In fact, the full multigrid algorithm converges the solution

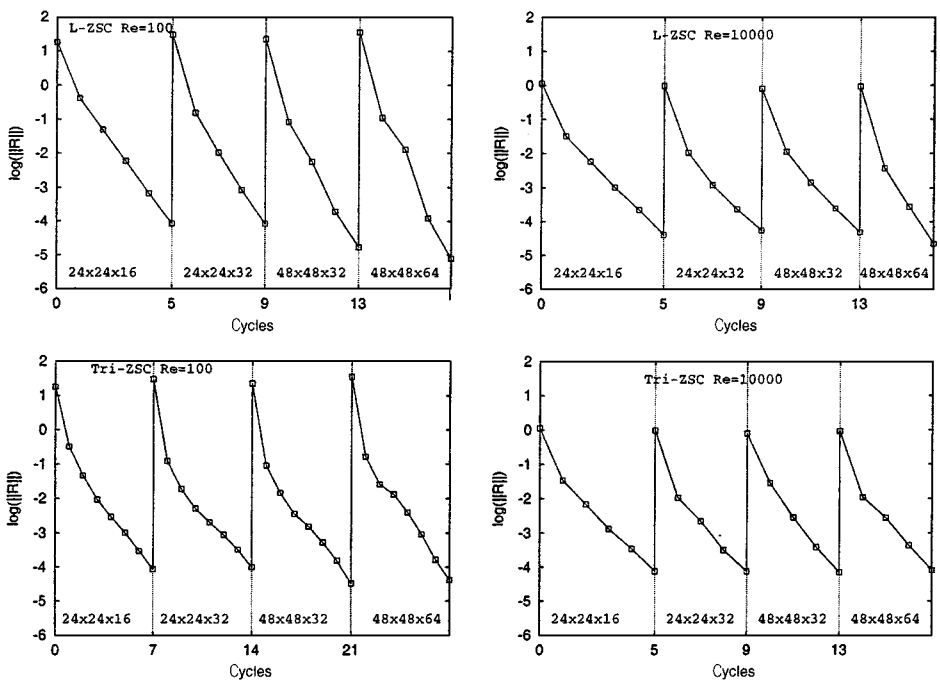

FIG. 12. L_2-norm of the residual versus F(2,1)-cycles with lexicographic (top graphs) and tri-plane (bottom graphs) xy-plane implicit smoothers combined with ZSC for several grids and Reynolds numbers.

TABLE IV

Average Convergence Factors Obtained in the Simulation of the Flat-Plate Problem for Several Stretched Grids, Reynolds Numbers, and F(2,1)-Cycles

	Grid			
	$24 \times 24 \times 32$		$48 \times 48 \times 64$	
Re	Tri-ZSC	L-ZSC	Tri-ZSC	L-ZSC
10^2	0.07	0.04	0.09	0.02
10^4	0.13	0.09	0.08	0.03

to below the truncation error with one F(2,1)-cycle per level. The asymptotic convergence rate is equal to 0.19, which is close to that obtained for the Poisson equation with the semi-coarsened approach [13].

Table IV shows the average convergence factors obtained in the simulation of the flat-plate problem for different F(2,1)-cycles and several stretched grids and Reynolds numbers. Although not included in this report, experiments with Reynolds numbers up to 10^6 were performed. Convergence rates, independent of the Reynolds number, the grid size, and the stretching factor, were achieved for the resolution of the boundary layer over a flat plate. Since the flow is aligned with the grid, the results obtained with the lexicographic and tri-plane smoothers are very similar. Furthermore the time per multigrid cycle is very similar for both smoothers (similar convergence per work unit). The parallel possibilities of tri-plane ordering make this approach more attractive. Results obtained for first-order accuracy (without QUICK correction) are even better. The residual norm is reduced by nearly five orders of magnitude in the first three cycles and the asymptotic convergence rate is equal to 0.1.

5. CONCLUSIONS AND FUTURE WORK

The robustness of two popular FAS multigrid algorithms (alternating-plane smoothers combined with full coarsening and plane smoothers combined with semi-coarsening) has been investigated through the solution of the incompressible 3-D Navier–Stokes equations. Convergence results have been obtained for two common benchmarks in CFD: the driven cavity and the flow over a flat plate. Robustness has been defined as the ability of the multigrid method to solve the model problem with a convergence rate per work unit independent of grid size, stretching factor, and Reynolds number (TMC).

The convergence factor has been shown to be independent of the grid size and stretching for the two robust approaches investigated in the driven-cavity simulation. Moreover, the convergence rate improves on stretched grids and for finer grids. The convergence is not Reynolds number independent and in fact the alternating-plane approach fails to converge for Reynolds numbers higher than 10^3. However, for lower Reynolds numbers, its convergence and operation count per cycle is better than that exhibited by the semi-coarsening approach. The difficult parallel implementation of the alternating-plane smoother and its difficulties in converging for high Reynolds numbers might make the semi-coarsening approach with tri-plane smooth ordering more attractive.

The combination of *xy*-plane smoothing and ZSC has been found to be the best choice for the flat-plate simulation. Its convergence rate is independent of grid size, stretching, and Reynolds number, and the tri-plane variant exhibits similar properties to the lexicographic ordering and allows the parallel implementation of the algorithm. The alternating-plane approach fails to converge in this case.

ACKNOWLEDGMENTS

We thank CSC (Centro de Supercomputación Complutense), ICASE, and the Computational Modeling and Simulation Branch at the NASA Langley Research Center for providing access to the parallel computers that have been used in this research.

REFERENCES

1. A. Brandt, *Multigrid Techniques: 1984 Guide with Applications to Fluid Dynamics*, Technical Report GMD-Studien 85 (May 1984).
2. A. Brandt, *Barriers to Achieving Textbook Multigrid Efficiency (TME) in CFD, ICASE Interim Report No. 32* (1998).
3. A. Brandt and I. Yavneh, On multigrid solution of high-Reynolds incompressible entering flows, *J. Comput. Phys.* **101**, 151 (1992).
4. J. E. Dendy, S. F. McCormick, J. W. Ruge, T. F. Russell, and S. Schafer, Multigrid methods for three-dimensional petroleum reservoir simulation, in *Tenth SPE Symposium on Reservoir Simulation, February 1989* (Society of Petroleum Engineers (SPE) 1989).
5. Joel H. Ferziger and Milovan Peric, *Computational Methods for Fluid Dynamics* (Springer-Verlag, Berlin/New York 1996).
6. T. Hayase, J. A. C. Humphrey, and R. Greif, A consistently formulated QUICK scheme for fast and stable convergence using finite-volume iterative calculation procedures, *Comput. Phys.* **98**, 108 (1992).
7. J. Linden, B. Steckel, and K. Stuben, Parallel multigrid solution of the Navier–Stokes equations on general 2-D domains, *Parallel Comput.* **7**, 461 (1988).
8. I. M. Llorente and N. D. Melson, Behavior of plane relaxation methods as multigrid smoothers, *Electron. Trans. Numer. Anal.* **10**, 92 (2000).
9. I. M. Llorente and F. Tirado, Relationships between efficiency and execution time of full multigrid methods on parallel computers, *IEEE Trans. Parallel Distrib. Systems* **8**(6), 562 (1997).
10. D. J. Mavriplis, *Multigrid Strategies for Viscous Flow Solvers on Anisotropic Unstructured Meshes*, Technical Report 98–6 (ICASE, 1998).
11. D. J. Mavriplis. *Large Scale Parallel Viscous Flow Computations Using and Unstructured Multigrid Algorithm*, Technical Report 99–44 (ICASE, 1999).
12. O. A. McBryan, P. O. Frederickson, J. Linden, A. Schüller, K. Solchenbach, K. Stüben, C. Thole, and U. Trottenberg, Multigrid methods on parallel computers—a survey of recent developments, *Impact Comput. Sci. Eng.* **3** (1991).
13. R. S. Montero, M. Prieto, I. M. Llorente, and F. Tirado, Robust multigrid algorithms for 3-D elliptic equations on structured grids, in *Proceedings of the 6th European Multigrid Conference (EuroMG'99), September 1999*, edited by E. Dick, K. Riemslagh, and J. Vierendeels (Springer-Verlag, Berlin/New York, 1999) p. 193.
14. W. Mulder, A new multigrid approach to convection problems, *J. Comput. Phys.* **83**, 303 (1989).
15. C. W. Oosterlee, The convergence of parallel multiblock multigrid methods, *J. Appl. Numer. Math.* **19**, 115 (1995).
16. C. W. Oosterlee, A GMRES-based plane smoother in multigrid to solve 3-D anisotropic fluid flow problems, *J. Comput. Phys.* **130**, 41–53 (1997).
17. C. W. Oosterlee, F. J. Gaspar, T. Washio, and R. Wienands, Multigrid line smoothers for higher order upwind discretizations of convection-dominated problems, *J. Comput. Phys.* **1**, 274 (1998).

18. A. K. Prasad and J. R. Koseff, Reynolds number and end-wall effects on a lid-driven cavity flow, *Phys. Fluids* **A1**, 208 (1989).
19. S. Schaffer, A semicoarsening multigrid method for elliptic partial differential equations with highly discontinuous and anisotropic coefficients, *SIAM J. Sci. Comput.* **20**, 228 (1998).
20. C. Thole and U. Trottenberg, Basic smoothing procedures for the multigrid treatment of elliptic 3d operators, *Appl. Math. Comput.* **19**, 333 (1986).
21. J. Thomas, B. Diskin, and A. Brandt, *Textbook Multigrid Efficiency for the Incompressible Navier–Stokes Equations: High Reynolds Number Wakes and Boundary Layers*, Technical Report 99–51 (ICASE, 1999).
22. M. C. Thompson and J. H. Ferziger, An adaptative multigrid technique for the incompressible Navier–Stokes equations, *J. Comput. Phys.* **82**, 94 (1989).
23. S. P. Vanka. Block-implicit multigrid solution of Navier–Stokes equations in primitive variables, *Comput. Phys.* **65**, 138 (1986).
24. P. Wesseling, *An Introduction to Multigrid Methods* (Wiley, New York, 1992).